CT-based assessment of 3D-printed clay elements

Alexander Chmelnizkij[1,3][0009−0004−7702−9829], Jasper Vollmert[1,3][0009−0001−6245−912X], Philipp Paetzold[2][0009−0004−1752−3913], Johannes Grün[2][0000−0002−9154−3929], Johannes Hagemann[2][0000−0003−2768−9496], Johannes Dora[2][0009−0001−4283−8499], Andreas Schropp[2][0000−0002−8846−8585], Kosmas Dragos[1][0009−0001−6245−912X], and Kay Smarsly[1,3][0000−0001−7228−3503)]

[1] Institute of Digital and Autonomous Construction, Hamburg University of Technology, Blohmstraße 15, 21079 Hamburg, Germany
`alexander.chmelnizkij@tuhh.de`
[2] Center for X-ray and Nano Science CXNS, Deutsches Elektronen-Synchrotron DESY, Notkestraße 85, 22607 Hamburg, Germany
[3] United Nations University (UNU) Hub on Engineering to Face Climate Change, United Nations University Institute for Water, Environment and Health (UNU-INWEH), Hamburg University of Technology, Germany

Abstract. Clay-based 3D printing has emerged as a low-carbon alternative to cementitious additive manufacturing in construction. However, pore space, inhomogeneities, shrinkage, and crack formation in clay-sand-water mixtures are still poorly understood, particularly with respect to their influence on the structural integrity of clay-printed elements. This paper investigates the use of X-ray computed tomography (CT) for specimen-scale analysis of clay-sand-water mixtures used in additive manufacturing. One printed specimen and two manually prepared reference specimens in the wet and dried state were scanned with the ENCI CT system. The reconstructed and segmented volumes were used to quantify pore volume, equivalent spherical diameter, sphericity, a derived specific pore surface, and spatial porosity distribution. The printed sample exhibited markedly smaller pores than the manually prepared dried sample, indicating compaction during extrusion and layer deposition, while the dried sample showed larger and more crack-like pores consistent with shrinkage during drying. Local porosity maps and their coefficients of variation were further used to identify heterogeneous zones that may act as mechanically weaker regions. The results demonstrate the feasibility of CT-based assessment for characterizing internal porosity and heterogeneity in 3D-printed clay elements.

Keywords: 3D clay printing · X-ray computed tomography · porosity · density distribution · structural integrity

1 Introduction

Sustainable construction methods have been attracting increasing attention due to the rising demand for low-carbon building materials and resource-efficient

ICCS Camera Ready Version 2026
To cite this paper please use the final published version:
DOI: 10.1007/978-3-032-29921-5_36

manufacturing processes [1]. As a low-carbon construction approach, clay-based additive manufacturing represents a low-carbon alternative to cement-based systems, since clay-based mixtures rely on locally available raw materials and low-temperature processes [2]. Clay printing, therefore, aligns with sustainability targets that include circular-economy principles and natural building materials in construction [3]. Nevertheless, for clay printing to constitute a viable alternative to cement-based construction, the properties of clay-printed elements must meet structural integrity requirements.

This study focuses on specimen-scale characterization based on X-ray computed tomography (CT) of representative material states in clay printing rather than on in-situ inspection of full-scale structures. Accordingly, the contribution of this work lies in a computational image-analysis workflow for pore segmentation, pore-size and pore-shape-related quantification, and spatial porosity mapping of clay-based specimens prepared from the same base mixture.

Structural integrity refers to the ability of a structural element to support its own weight and external loads, which is crucial for civil engineering structures, ensuring stability, functionality, and safety over time. To ensure the structural integrity of clay-printed (additively manufactured) elements, to be used as load-bearing elements, reliable assessment of the element mechanical properties is required [4]. For example, material-related uncertainties, which directly affect the mechanical properties, may limit the deployment of clay-printed elements, because shrinkage-induced cracking and internal inhomogeneities can reduce the load-bearing capacity. Mixture composition, including clay-sand ratio and water content, influences the mechanical properties, while reliable relationships between mixture parameters, internal quality, and failure behavior have yet to be sufficiently established.

In recent years, 3D printing quality has become the focus of increasing research efforts. For example, research on 3D concrete printing has reported on establishing links between mixture design, process parameters, and compressive strength, often supported by standardized mechanical testing and process monitoring [5, 6]. Furthermore, research on earthen construction and clay materials has provided an improved understanding of shrinkage, drying-induced cracking, and moisture-dependent strength [7]; however, the transfer to layered-extrusion processes of clay printing remains incomplete. Research on clay-based additive manufacturing has reported recurring variability in printing quality, including void formation and strength scatter, which indicates a need for systematic internal characterization of clay-printed elements beyond surface inspection. In this context, computed tomography has been used for investigating the internal material structure of cementitious materials [8]. CT application in clay-based additive manufacturing has been limited, leaving open questions regarding the internal structure, homogeneity, and layer interfaces of clay-printed elements at scales of interest.

Quantitative, spatially resolved methods for evaluating porosity and material distribution in clay-printed elements have been scarce. Consequently, the safety assessment, reliability evaluation, and scalable process qualification in construc-

ICCS Camera Ready Version 2026
To cite this paper please use the final published version:
DOI: 10.1007/978-3-032-29921-5_36

tion of clay-based additive manufacturing are limited, thus hindering the understanding of the contribution of inhomogeneities, drying-induced defects, and load-induced crack growth to failure mechanisms. This paper reports on a feasibility study that uses employing CT scanning, for visualizing and analyzing internal structures in macroscopic clay-printed elements. The study employs the "extracting non-destructively cuneiform inscriptions" (ENCI) mobile X-ray CT scanner [9–11], originally developed for on-site investigation of cultural heritage objects. Volumetric reconstructions from CT scanning results and segmentations capture the pore space and potential weak zones in the samples, as well as potential geometric discontinuities. The CT scanning, volumetric reconstruction, and segmentation are applied to three samples, one "wet", one "dried", and one "printed" sample, representing the main material states during processing. The wet and dried reference samples were prepared separately from the same base mixture by manual mixing and were not 3D-printed. The printed sample is processed as wet material in 3D printing and then left to dry at approximately 19°C and relative humidity of 30%, whereas the wet and dried samples are prepared separately and not 3D-printed, enabling investigation of the influence of the printing process on the material. For visualization, the CT scanning results are rendered, revealing potential weak zones for the structural integrity of each sample.

The remainder of this paper is structured as follows. Section 2 describes the design and implementation of the feasibility study, including sample preparation, CT scanning, and volumetric reconstruction. Section 3 presents the segmentation and evaluation of pore spaces, detailing the pore identification workflow and quantitative descriptors (e.g., pore-size distributions and shape measures) for comparing the wet, dried, and printed samples. Section 4 reports the volume-rendering results and analyzes the spatial porosity distribution to localize regions of elevated porosity within each sample. Section 5 summarizes the main findings and outlines future work toward CT-based quality assessment of clay-printed elements.

2 Design and implementation

This section describes the design and implementation of the feasibility study. First, the preparation of samples is discussed, followed by the CT scanning process and volumetric reconstruction.

2.1 Sample preparation

Clay-printed elements undergo different states throughout the printing process. The porosity and its effects on the mechanical properties of the elements concern both the wet state, i.e. during printing, as well as the dry state, i.e. after the element has dried. The CT scanning process is applied to the three types of samples, previously described. The non-printed samples (wet and dried) are extracted as cylindrical shapes, upon manual mixing of raw materials. To reduce

ICCS Camera Ready Version 2026
To cite this paper please use the final published version:
DOI: 10.1007/978-3-032-29921-5_36

water demand and improve mechanical stability, a binder based on modified starch is added to the mixture. The binder has a bulk density of 0.5 g/cm$^{\mathbf{3}}$ and increases the breaking strength of the material. The volumetric composition of the mixture consists of 29% clay, 43% sand, 27.5% water, and 0.5% binder. The addition of sand to the mixture is intended to mitigate the shrinkage of the clay during the drying process. However, the addition of sand is kept relatively low, since increased sand quantities may compromise the cohesive strength of the clay. The same clay-sand-water-binder mixture is used for all three samples. The dried reference sample is stored for 48 h in a construction container under practical site-like ambient conditions. Temperature is not continuously tracked, but day-night fluctuations range approximately from 7 °C at night to 13.5 °C during daytime. Relative humidity and sample mass loss are not monitored. This conditioning is chosen to reflect realistic construction-site conditions, but it also limits strict reproducibility of the drying protocol. The grain size of the sand ranges from 0.062 mm to 0.3 mm to achieve a well-graded and compactable particle size distribution. The grain size distributions of the sand and the clay are shown in Figure 1 on a logarithmic scale. The chemical composition[1] and bulk density of the clay material and the sand are summarized in Table 1.

Table 1. Density and chemical composition of utilized clay and quartz sand.

	Clay	Quartz sand
Bulk density [g/cm^3]	2.65	1.3
Chemical analysis [%]		
SiO_2	70.50	92.12
Al_2O_3	23.50	2.71
TiO_2	1.6	0
Fe_2O_3	1.00	0.10
CaO	0.10	0.93
MgO	0.40	0.22
K_2O	2.80	1.46
Na_2O	0.10	0.16
Others	0	2.3

The dried sample is exposed to ambient air to allow drying, while the wet sample is sealed to preserve its moisture content (foil insulation). For the printed sample, a wave-like hollow cylinder with a diameter of approximately 5 cm and a height of 10 cm is printed using a Potterbot Scara v4 robot equipped with a linear-ram extruder and 4000 ml extrusion tubes. The material is deposited through a nozzle with a diameter of 9 mm at a printing speed of 20 mm/s and a layer height of 3.5 mm. The installation of the printed sample in the CT scanner is illustrated in Figure 2(left), and the CT scanning process is described in the next subsection.

---

[1] Reported values are taken from the available chemical analysis; minor constituents not separately quantified are grouped as "Others".

ICCS Camera Ready Version 2026
To cite this paper please use the final published version:
DOI: 10.1007/978-3-032-29921-5_36

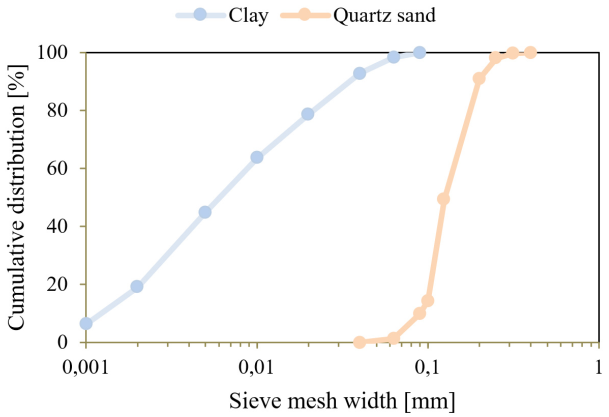

Fig. 1. Cumulative grain size distribution of clay and quartz sand.

2.2 CT scanning process

The prepared samples are examined using the mobile CT scanner ENCI. During acquisition, each specimen is mounted on a flat sample holder and laterally stabilized with supporting rods to prevent positional shifts throughout the rotational scan. All samples are measured using identical device parameters to ensure direct comparability of the reconstructed volumes.

The imaging geometry follows a cone-beam configuration with an almost threefold geometric magnification, achieved by a source-to-detector distance of 308.81 mm and a source-to-sample distance of 103.64 mm. X-ray generation is performed at an acceleration voltage of 180 kV and a tube current of 400 µA. To suppress beam-hardening artefacts caused by the polychromatic spectrum of the X-ray tube, a 2 mm copper filter is applied, effectively pre-hardening the beam and improving quantitative image quality.

Data acquisition is conducted in continuous scanning mode using 2881 projections (3072x1944 pixel) with an exposure time of 0.3 s per projection, resulting in a total scan time of less than 15 minutes for a full 360° rotation. The dataset is subsequently processed using twofold binning and is cropped to the relevant field of view. While binning reduces the effective spatial resolution, it significantly enhances the signal-to-noise ratio.

For the wet sample, the protective foil insulation is intentionally retained during scanning to preserve the native state of the material. Figure 2(right) shows the ENCI CT scanner with the scanning chamber open and the positioned sample prior to measurement.

2.3 Reconstruction procedure

To obtain volumetric information about the internal structure of the samples, the acquired projection data are reconstructed using a cone-beam filtered back-projection workflow based on the Feldkamp–Davis–Kress (FDK) algorithm for

ICCS Camera Ready Version 2026
To cite this paper please use the final published version:
DOI: 10.1007/978-3-032-29921-5_36

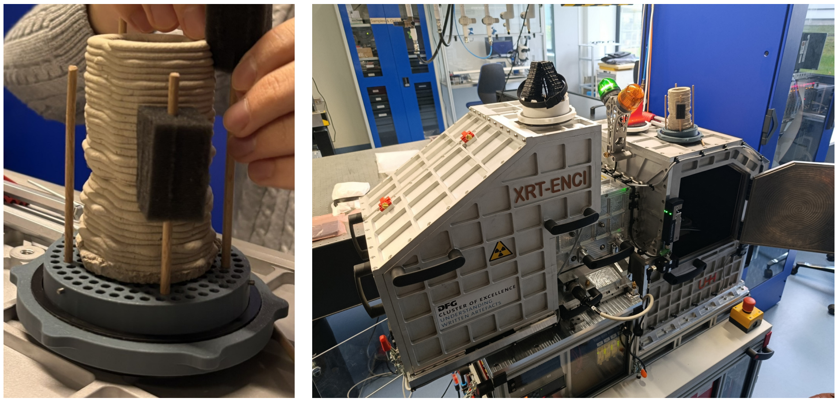

Fig. 2. Installation of the printed sample on the sample mount(left).The ENCI CT scanner with the scanning chamber open and the printed sample to be examined(right).

circular trajectories [13]. The analytical reconstruction method provides an efficient and robust solution for three-dimensional cone-beam geometries and is widely established in high-resolution laboratory CT.

The reconstruction is performed on an NVIDIA A100 GPU, enabling a total reconstruction time of approximately 10 minutes despite the large dataset size. The resulting volume is represented as a Cartesian voxel grid, where each voxel intensity corresponds to the local X-ray attenuation coefficient encoded as a gray-value scalar within a three-dimensional array. A comprehensive mathematical treatment of tomographic reconstruction and discretized volume representations can be found in [14].

Figure 3 presents an example cross-section of the dried cylindrical sample, illustrating the achievable contrast and spatial resolution. The reconstructed volumes subsequently serve as the basis for pore-space segmentation and quantitative structural analysis, as described in the following section.

3 Segmentation and evaluation of pore spaces

The segmentation of the reconstructed images is applied for enabling pore identification, thus facilitating the analysis of pore spaces. In this section, first, the segmentation process is explained, followed by the pore identification for all samples.

3.1 Segmentation

Segmentation facilitates the identification of regions within the CT data exhibiting a notable contrast. The Dragonfly 3D World software [15] employs an automatic porosity segmentation technique based on the advanced Otsu's method [16]. In this method, a region of interest is first defined for the material using the

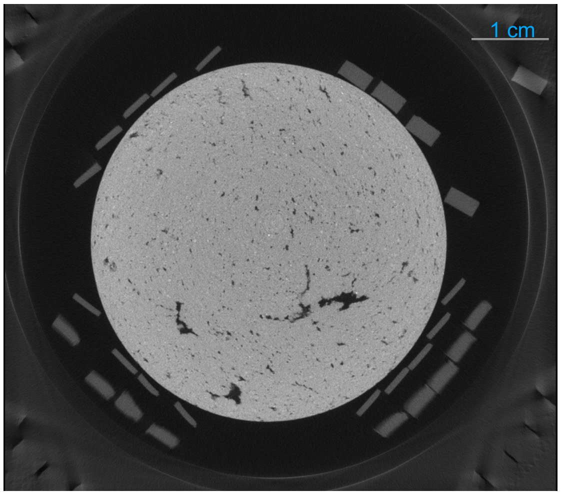

Fig. 3. Reconstructed CT cross-section of the dried cylindrical sample.

upper Otsu threshold. Internal pores are then identified, and a dilate operation is applied using a 3D kernel with a size of 5×5×5 voxels to increase the region of interest (ROI) beyond the edge of the segmented material. The ROI is then split at the Otsu threshold to effectively separate the pores from the segmented material. In addition to the density-based criteria for defining ROIs, connectivity constraints are applied to exclude spurious pore detections at the voxel scale and to retain only physically meaningful pores. Contiguous segments are evaluated using a 6-connected neighborhood (face connectivity), and isolated components smaller than nine voxels are removed. The initial phase of the procedure involves the examination of the dried and wet cylindrical samples for segmentation purposes. To remove structurally irrelevant small pores, a minimum equivalent spherical diameter threshold of 1 mm is applied. In the following, cubic portions of the cylindrical samples illustrated in Figure 4 are examined to circumvent the influence of boundary effects on the pore space geometry of the samples.

3.2 Pore identification and analysis of pore spaces

Upon completing the segmentation, the pores are identified and analyzed in 3D. Figure 5 shows a cross-sectional analysis of the wet and dried samples, the analysis of which reveals divergent characteristics. The pores of the wet sample are more rounded in shape than the pores of the dried sample, which exhibit crack-like pores, as a result of the drying process and the associated shrinkage of the sample. Furthermore, the wet sample contains more small spherical pores than the dried sample, in which it is conjectured that small pores are barely discernible after shrinkage. Color coding indicates pore volume and facilitates estimation of pore size.

ICCS Camera Ready Version 2026
To cite this paper please use the final published version:
DOI: 10.1007/978-3-032-29921-5_36

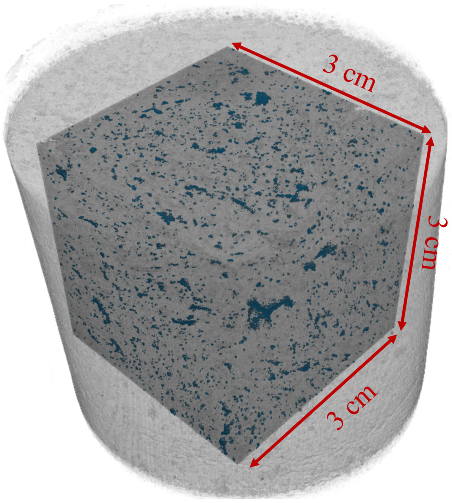

Fig. 4. Exemplary cubic element of the dried sample.

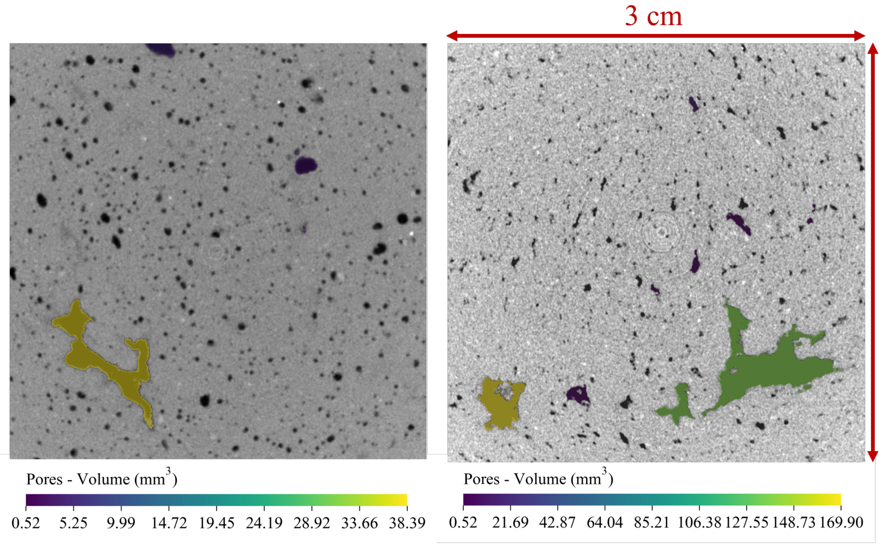

Fig. 5. Segmentation results of the pores with respect to volume of the wet (left) and dried (right) samples. The circular structure near the center is a reconstruction-related ring artefact.

ICCS Camera Ready Version 2026
To cite this paper please use the final published version:
DOI: 10.1007/978-3-032-29921-5_36

The analysis of pore volumes for the wet, dried and printed samples reveals discrepancies in the distribution of pore sizes. As illustrated in the histogram of Figure 6, the dried sample contains several large pores, with a size greater than 40 mm$^{\mathbf{3}}$. By contrast, in the wet sample no pores exceeding 40 mm^3 are identified. All the pores of the printed sample are smaller than 5 mm$^{\mathbf{3}}$, indicating that the clay printing process results in considerable compaction of the material during the extrusion process.

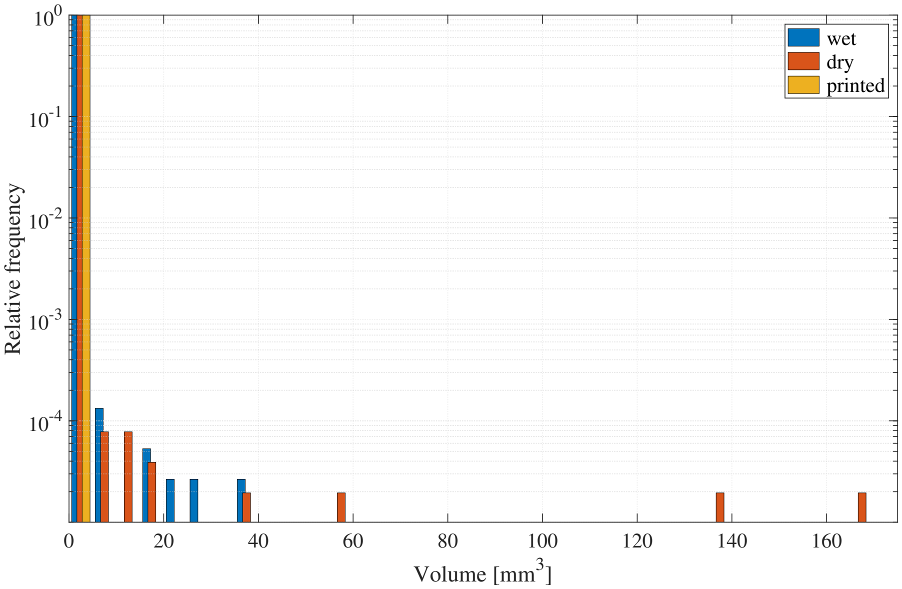

Fig. 6. Histogram of pore volumes for the wet, dried, and printed samples (bin width 5 mm^3).

Pore shape is quantified by the so-called “sphericity”, which examines the spherical similarity of each pore on a scale from 0 to 1. As demonstrated in Figure 7, the results of the sphericity calculation for the samples indicate that the majority of the wet-sample pores exhibit a high degree of spherical similarity, most of which lie close to 1. The high sphericity of the wet sample is attributed to the presence of pore water resisting pore deformations. In addition, the non-spherical pores observed in the dried and printed samples are attributed to the shrinkage that occurs during the drying process. Further insights into pore shape deviations and spatial porosity distribution are obtained from volume renderings of the CT data, as described in the following subsection.

It can be posited that the high sphericity is attributable to the pore water in the wet sample resisting pore deformations. Additionally, the non-spherical pores observed in the dried and printed samples can be attributed to the shrinkage that occurs during the drying process.

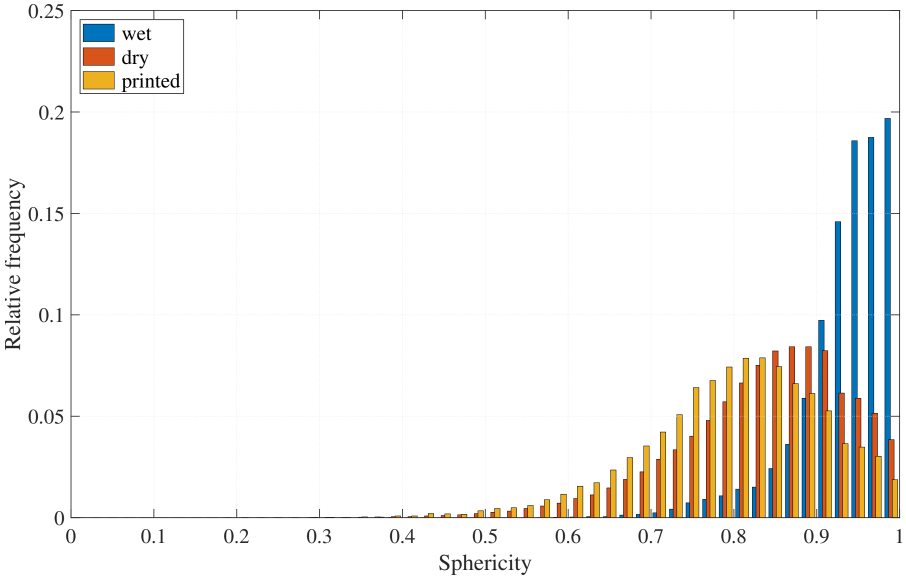

Fig. 7. Distribution of sphericity values for the wet, dried, and printed samples.

As a supplementary pore descriptor, the derived specific pore surface A/V is computed from the sphericity Φ and the equivalent spherical diameter d_{eq} as

$$\frac{A}{V} = \frac{6}{\Phi\, d_{\mathrm{eq}}}. \quad (1)$$

The mean derived specific pore surface A/V is 28.93 ± 10.37 mm^{-1} for the wet sample, 39.37 ± 10.15 mm^{-1} for the dried sample, and 38.38 ± 8.87 mm^{-1} for the printed sample, where the standard deviation $\pm\sigma$ reflects the variability of pore geometries within each sample. These results complement the sphericity analysis and indicate more compact pore geometries in the wet sample and less compact, more irregular pore geometries in the dried and printed samples.

The subsequent section will examine the shapes of the pores and the spatial distribution of the porosity. In addition, a use case will be presented, in which the data obtained in this study will be employed for numerical investigations of the structures under load.

4 Rendering and spatial porosity

Rendered views are generated from reconstructed CT data to support qualitative assessment of internal features and to guide subsequent quantitative analyses. Dragonfly software [15] is used for rendering, with linear interpolation applied to the data. A general foundation explaining volume visualization and transfer-function design is provided by [17], while an application-oriented overview of

ICCS Camera Ready Version 2026
To cite this paper please use the final published version:
DOI: 10.1007/978-3-032-29921-5_36

volume rendering methods is summarized by [18]. Figure 8 shows the volume rendering results for the wet and dried samples. The pores are colored by volumetric size, corroborating the observations in the previous subsection, regarding the high sphericity of the wet sample. Moreover, the non-spherical pores of the dried sample are characterized by torn, crack-like shapes, supporting the hypothesis of crack formation in the pores due to shrinkage in the drying process. Furthermore, the volume rendering of the printed sample is shown in Figure 9. The pores in the printed sample are aligned parallel to the horizontal layer direction, introducing porosity-induced anisotropy within the material. Larger pores occur at relatively low frequencies and are preferentially located and aligned along inter-layer boundaries. Only a few pores of size smaller than 2.71 mm^3 are distributed over the sample volume, highlighting the material compaction during the clay printing process.

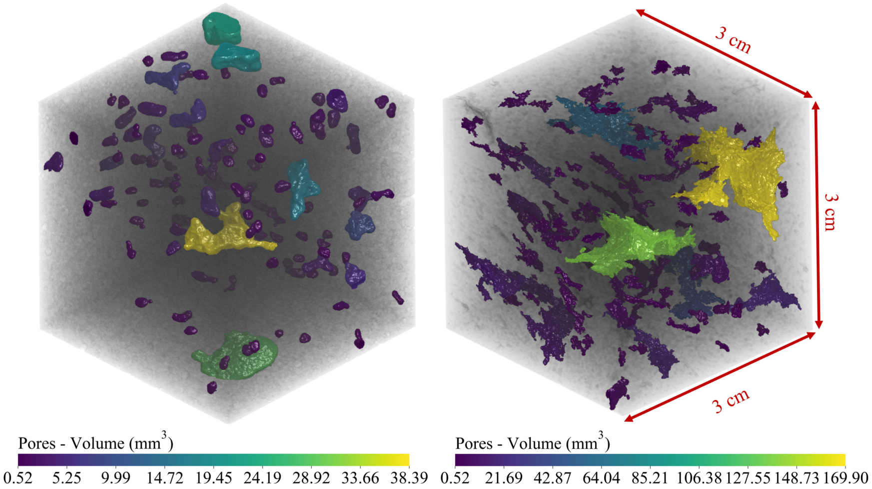

Fig. 8. Rendered pores of the wet (left) and dried (right) samples.

Despite the evident decrease of pore size for the printed sample, which enhances the structural integrity of the material, the spatial distribution of the pores is also crucial for the behavior of the sample under loading. To assess the structural integrity, the samples are subdivided into cubic elements and evaluated in terms of the volumetric contribution of each pore to the total volume of each sample. The cubic elements are of 1000 $\mathbf{mm^3}$ volume, and the porosity is determined within each cubic element. The resulting volume of the solid material in each cubic element is illustrated in Figure 10 for the wet and dried samples. A similar procedure is applied to determine the porosity of the printed sample, as shown in Figure 11, for wedge-like elements.

The analysis of the spatial porosity distribution of the dried sample reveals regions of diminished solid volume, indicated by the presence of yellow areas,

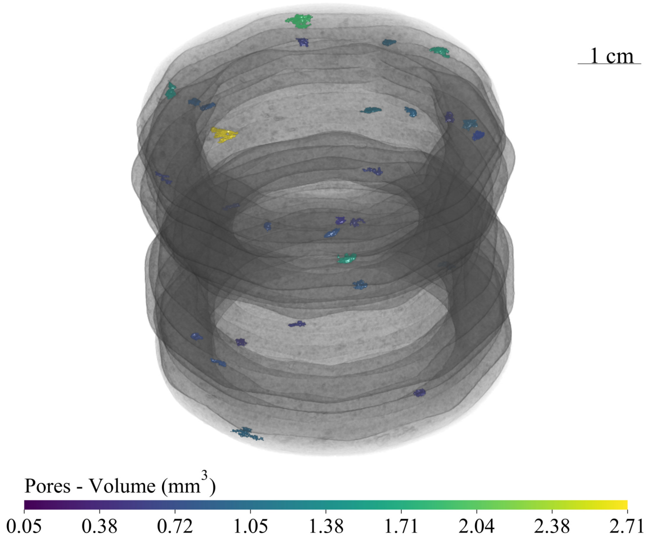

Fig. 9. Rendered pores of the printed sample.

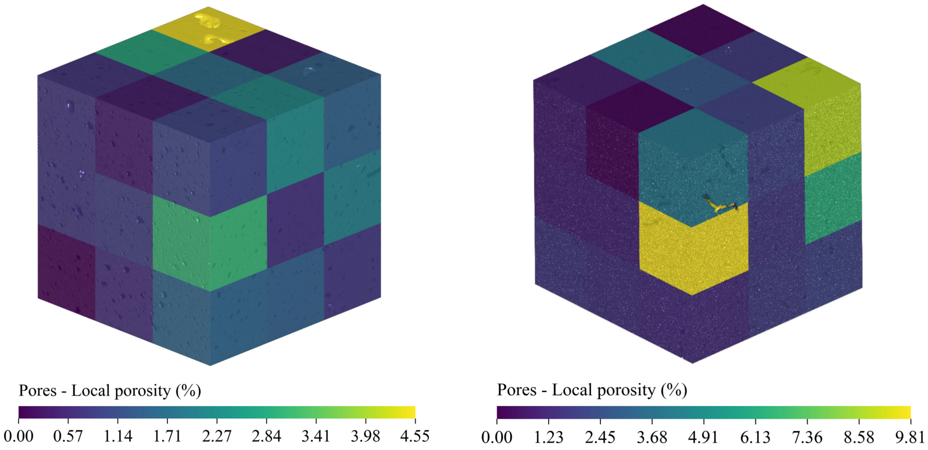

Fig. 10. Spatial porosity distribution of the wet (left) and dried (right) samples.

ICCS Camera Ready Version 2026
To cite this paper please use the final published version:
DOI: 10.1007/978-3-032-29921-5_36

which are potentially vulnerable during loading. Regarding the printed sample, the yellow and green regions indicate potentially critical zones under loading due to their elevated local porosity. The elevated porosity near the top layer may be related to the absence of compaction by subsequently deposited layers and/or to different drying conditions at the exposed surface. This interpretation remains a hypothesis and should be examined in future work using repeated specimens and controlled environmental conditions.

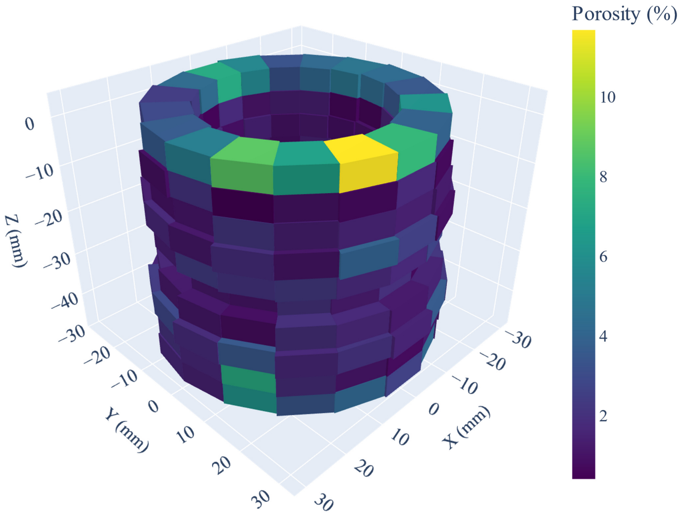

Fig. 11. Spatial porosity distribution of the printed sample (bin width 10° and 5 mm height).

The present study analyzes one sample per condition (wet, dried, printed) and therefore primarily demonstrates methodological feasibility rather than statistical representativeness. The selected samples are representative of the three relevant processing states and were prepared from the same base mixture, which enables a meaningful qualitative comparison. At the same time, the drying conditions were intentionally site-like rather than laboratory-controlled. The reported pore descriptors should therefore be interpreted as indicative trends rather than population-level values.

5 Conclusions and future work

In this paper, a feasibility study has been presented, demonstrating that mobile X-ray CT scanning serves as an effective non-destructive approach for identifying and quantifying pore geometries in clay-printed elements. The CT scanning has

ICCS Camera Ready Version 2026
To cite this paper please use the final published version:
DOI: 10.1007/978-3-032-29921-5_36

been applied to three clay-based samples: one wet, one dried, and one printed sample, representing the material states that the mixture exhibits during printing and drying. Segmentation analyses of the CT results have yielded findings on pore morphologies and distributions that are consistent with the expected porosity characteristics of each specimen. Specifically, relatively small pores in the wet specimen have been observed to be of primarily spherical shapes, while the dried specimen has exhibited large, crack-like pores, as a result of clay shrinkage. The printed sample has also shown crack-like pores, but much smaller in comparison to the dried sample, which is attributed to compaction during the printing process. Furthermore, compaction by subsequently deposited layers appears to have resulted in smaller pores in the lower layer. The segmentation findings have been further corroborated by volume rendering of the CT scanning results. In future research, the concept presented in this feasibility study may be extended to large sets of specimens with varied mixture parameters, coupled with mechanical testing, to establish reliable correlations between internal structure of clay-printed elements and load-bearing performance. Furthermore, geometry-informed numerical models may be established for structural analysis.

Acknowledgments. The authors gratefully acknowledge financial support received from the German Research Foundation (DFG) through grants SM 281/31-1, SM 281/33-1, and SM 281/44-1 as well as from Hamburg University of Technology under the I^3 Program through the junior project "Digitalization of earth printing to advance climate-informed engineering". Further support has been provided by Hi-Acts, an innovation platform funded by Helmholtz Association (HGF). The authors also thank HC HAGEMANN GmbH & Co. KG (Hamburg, Germany) for providing the facilities for the clay-printing laboratory essential to this study. The research for the CT scanning is funded by DFG under Germany's Excellence Strategy – EXC 2176 'Understanding Written Artefacts: Material, Interaction and Transmission in Manuscript Cultures', project no. 390893796. Any opinions, findings, conclusions, or recommendations expressed in this paper are those of the authors and do not necessarily reflect the views of the aforementioned sponsors.

Disclosure of Interests. No competing interests are declared.

References

1. Rocha, D., Faria, P., Lucas, S.S.: Additive Manufacturing of Earth-Based Materials: A Literature Review on Mortar Composition, Extrusion, and Processing Earth. Materials **17**(1), 202 (2023). https://doi.org/10.3390/ma17010202
2. De Witte, D.: Clay Printing: The Fourth Generation Brickwork. Mechanik, Werkstoffe und Konstruktion im Bauwesen, vol. 62. Springer Fachmedien Wiesbaden, Wiesbaden (2022). https://doi.org/10.1007/978-3-658-37161-6
3. Curth, A., Pearl, N., Castro-Salazar, A., Mueller, C., Sass, L.: 3D printing earth: Local, circular material processing, fabrication methods, and Life Cycle Assessment. Constr. Build. Mater. **421**, 135714 (2024). https://doi.org/10.1016/j.conbuildmat.2024.135714

ICCS Camera Ready Version 2026
To cite this paper please use the final published version:
DOI: 10.1007/978-3-032-29921-5_36

4. Asaf, O., Bentur, A., Larianovsky, P., Sprecher, A.: From soil to printed structures: A systematic approach to designing clay-based materials for 3D printing in construction and architecture. Constr. Build. Mater. **408**, 133783 (2023). https://doi.org/10.1016/j.conbuildmat.2023.133783
5. Mishra, S.K., Snehal, K., Das, B.B., Chandrasekaran, R., Barbhuiya, S.: From printing to performance: A review on 3D concrete printing processes, materials, and life cycle assessment. J. Build. Pathol. Rehabil. **10**(2) (2025). https://doi.org/10.1007/s41024-025-00626-4
6. Farrokhsiar, P., Gursoy, B., Duarte, J.P.: A comprehensive review on integrating vision-based sensing in extrusion-based 3D printing processes: Toward geometric monitoring of extrusion-based 3D concrete printing. Constr. Robot. **8**(2), 21 (2024). https://doi.org/10.1007/s41693-024-00133-x
7. Dorresteijn, E., Tsiotou, S., Lowke, D.: Keeping the Processability of a Clay Mortar for Extrusion 3D Printing While Decreasing Shrinkage and Increasing the Green Strength. In: Beckett, C., Bras, A., Fabbri, A., Keita, E., Perlot, C., Perrot, A. (eds.) Second RILEM International Conference on Earthen Construction, RILEM Bookseries, vol. 52, pp. 42–51. Springer Nature Switzerland, Cham (2024). https://doi.org/10.1007/978-3-031-62690-6_5
8. Mohan, M.K., Rahul, A.V., Van Stappen, J.F., Cnudde, V., De Schutter, G., Van Tittelboom, K.: Assessment of pore structure characteristics and tortuosity of 3D printed concrete using mercury intrusion porosimetry and X-ray tomography. Cem. Concr. Compos. **140**, 105104 (2023). https://doi.org/10.1016/j.cemconcomp.2023.105104
9. Michel, C., Schroer, C. G., Olbrich, S., Beckert, A., Ehteram, S. Schropp, A., Paetzold, P., Döhrmann, R., Wiljes, P., Botta, S., Bohn, M., Zerbe, K., Aksoy, A.: Deciphering 4,000-year-old cuneiform letters hidden in clay envelopes using a mobile X-ray computed tomography scanner (submitted).
10. Paetzold, P., Ehteram, S., Krämer, L., Isensee, F., Schropp, A., Schroer, C. G., Gippert, J.: Non-Destructive Investigation of a Georgian Codex Binding Using a Portable Computed Tomography Scanner, Digital Kartvelology **4**, 75–84 (2025). https://doi.org/10.62235/dk.4.2025.10509
11. Olbrich, S., Beckert, A., Michel, C., Schroer, C. G., Ehteram, S., Schropp, A., Paetzold, P.: Efficient Analysis and Visualization of High-Resolution Computed Tomography Data for the Exploration of Enclosed Cuneiform Tablets, IEEE 14th Symposium on Large Data Analysis and Visualization (LDAV), (2024). https://doi.org/10.1109/LDAV64567.2024.00012
12. Sulsky, D., Chen, Z., Schreyer, H.L.: A particle method for history-dependent materials. Computer Methods in Applied Mechanics and Engineering **118**(1–2), 179–196 (1994)
13. Feldkamp, L.A., Davis, L.C., Kress, J.W.: Practical cone-beam algorithm. Journal of the Optical Society of America A **1**(6), 612–619 (1984)
14. Kak, A.C., Slaney, M.: Principles of Computerized Tomographic Imaging. IEEE Press, New York (1988)
15. Comet Technologies Canada Inc.: Dragonfly 3D World Help (Version 2024.1): Image Properties and Settings. https://www.dragonfly.com, last accessed 2024/01/01
16. Otsu, N.: A threshold selection method from gray-level histograms. IEEE Transactions on Systems, Man, and Cybernetics **9**(1), 62–66 (1979)
17. Levoy, M.: Display of surfaces from volume data. IEEE Computer Graphics and Applications **8**(3), 29–37 (1988)
18. Engel, K., Hadwiger, M., Kniss, J.M., Rezk-Salama, C., Weiskopf, D.: Real-Time Volume Graphics. AK Peters, Natick (2006)

ICCS Camera Ready Version 2026
To cite this paper please use the final published version:
DOI: 10.1007/978-3-032-29921-5_36